

Multidimensional Ordered Bifunctional Air Electrode Enables Flash Reactants Shuttling for High-Energy Flexible Zn-Air Batteries

*Yi Jiang, Ya-Ping Deng, Ruilin Liang, Jing Fu, Dan Luo, Guihua Liu, Jingde Li, Zhen Zhang, Yongfeng Hu, and Zhongwei Chen**

Direct growth of electrocatalysts on conductive substrates is an emerging strategy to prepare air electrodes for flexible Zn-air batteries (FZABs). However, electrocatalysts grown on conductive substrates usually suffer from disorder and are densely packed with “prohibited zones”, in which internal blockages shut off the active sites from catalyzing the oxygen reaction. Herein, to minimize the “prohibited zones”, an ordered multidimensional array assembled by 1D carbon nanotubes and 2D carbon nanoridges decorated with 0D cobalt nanoparticles (referred as MPZ-CC@CNT) is constructed on nickel foam. When the MPZ-CC@CNT is directly applied as a self-supported electrode for FZAB, it delivers a marginal voltage fading rate of 0.006 mV cycle⁻¹ over 1800 cycles (600 h) at a current density of 50 mA cm⁻² and an impressive energy density of 946 Wh kg⁻¹. Electrochemical impedance spectroscopy reveals that minimal internal resistance and electrochemical polarization, which is beneficial for the flash reactant shuttling among the triphase (i.e., oxygen, electrolyte, and catalyst) are offered by the open and ordered architecture. This advanced electrode design provides great potential to boost the electrochemical performance of other rechargeable battery systems.

Nevertheless, unsatisfactory rechargeability and energy efficiency as a result of the sluggish oxygen reaction kinetics in the air electrode still significantly hinder the applications of flexible ZABs (FZABs). A high-performance bifunctional air electrocatalysis system, designed for both oxygen reduction reaction (ORR), while discharging and oxygen evolution reaction (OER) during charging, is the key to break through these obstacles. As a result, extensive research efforts have been carried out to optimize bifunctional air electrode in order to boost both the ORR and OER kinetics for the high performance FZABs.^[4,13–16]

A most typical strategy to optimize the electrode performances is to composite transition-metal-based materials (oxides, chalcogenides, phosphides, and nitrides) with heteroatom-doped carbon nanomaterials.^[10,14,17–22] However, several critical issues remain unaddressed. First and

foremost, the hybrid components chemically deposited grown on the conductive substrates usually present random orientation and densely packed aggregation, which inevitably generates abundant “prohibited zones”, which describes the buried zones within the air electrodes that lost their electrocatalytic activity due to reactants inaccessibility.^[23–26] The corresponding functionality loss of catalysts significantly impedes the overall capability of FZABs, especially at large currents or high bending angles. Secondly, intrinsic activity of electrocatalytic sites in state-of-the-art flexible air electrode is still insufficient in providing the desirable performance. Although increasing catalyst loading can improve battery performance, it simultaneously increases charge impedance, deters oxygen penetration, and promotes active material detachment.^[27,28] Thirdly, hybrid catalysts frequently struggle to maintain their highly dispersed state for long period of operation, owing to inevitable carbon support corrosion and subsequent aggregation of the transition metal-based nanoparticles.^[29–31] This deficiency may undergo further aggravation as the FZABs are cycled under large currents or tested under extreme shape deformations.^[32,33]

Herein, to overcome the aforementioned disadvantages, an array with limited “prohibited zones” assembled by 1D carbon nanotube (CNT) and 2D carbon nanoridge decorated with

1. Introduction

Flexible electrochemical energy conversion and storage systems are under blooming development in the last decade.^[1–7] Particularly, Zn-air batteries (ZABs) with superiorities of high theoretical energy density (1218 Wh kg⁻¹), low cost, and high safety possess remarkable potential to meet the increasing practical requirements of flexible and wearable electronics.^[8–13]

Dr. Y. Jiang, Y.-P. Deng, R. Liang, Dr. J. Fu, D. Luo, G. Liu, Dr. J. Li, Z. Zhang, Prof. Z. Chen
 Department of Chemical Engineering
 Waterloo Institute for Nanotechnology
 Waterloo Institute for Sustainable Energy
 University of Waterloo
 Waterloo, Ontario N2L 3G1, Canada
 E-mail: zhwchen@uwaterloo.ca

Dr. Y. Hu
 Canadian Light Source
 University of Saskatchewan
 Saskatoon, Saskatchewan S7N 0 X 4, Canada

 The ORCID identification number(s) for the author(s) of this article can be found under <https://doi.org/10.1002/aenm.201900911>.

DOI: 10.1002/aenm.201900911

0D cobalt nanoparticle (MPZ-CC@CNT) is directly grown on arbitrary conductive substrates. The CNT with high-level of N dopants is in situ sprouted from the highly dispersed cobalt seeds during pyrolysis of the 2D ZnCo bimetal coordination framework, which forms the open and ordered arrays. The as-generated architecture enables flash cycling of reactants toward and away from catalytic sites at the gas–solid–liquid triphasic interfaces for enhanced reaction frequency, resulting in superior electrocatalytic kinetics evidenced by electrochemical measurements. Furthermore, the space-confined CNTs aid to alleviate cobalt nanoparticles agglomeration, which guarantees long-lasting stability at high current density. Attributed to these superiorities, the FZAB fabricated using the self-supported MPZ-CC@CNT electrode demonstrates pronounce electrochemical performance and mechanical flexibility.

2. Results and Discussion

2.1. Synthesis and Characterization

The synthetic process of MPZ-CC@CNT can be divided into three major steps as schemed in **Figure 1**. First, Zn-hexamine (Zn-HMT) is seeded and sprouted into a well-aligned array on the skeleton of the nickel foam (NF) substrate (Figure S1a–c, Supporting Information). The identity of the deposited material is confirmed by X-ray diffraction (XRD) pattern of the as-prepared Zn-HMT@Ni and powder sample scraped from the substrate, which agrees with pattern of previously reported Zn-HMT coordination frameworks.^[34] The uniform color change from pristine metallic silver to white of the substrate

also indicates the homogeneous rootage of the Zn-HMT on substrate (Figure S2a, b, Supporting Information). It is worth mentioning that these 2D coordination frameworks can be successfully adapted onto other substrates, such as stainless-steel mesh, Zn foil, and carbon cloth (Figure S3, Supporting Information), demonstrating the versatility of the proposed synthetic strategy. In the second step, a cation-exchange process is used to convert the Zn-HMT with smooth surface (Figure S1, Supporting Information) into ZnCo-HMT coordination frameworks that exhibit rough surface morphology without changing the overall 2D architecture (**Figure 2a, b, e**, and **Figure S4**, Supporting Information). This reaction is accompanied by a distinct color change from white to purple (Figure S2c, Supporting Information). In addition, the presence of Zn, Co, and N are confirmed by X-ray photoelectron spectroscopy (XPS) and energy dispersive X-ray spectroscopy (Figures S5 and S6, Supporting Information).

Finally, a chemical-vapor deposition (CVD) process using acetonitrile as carbon and nitrogen source is performed during pyrolysis of the ZnCo-HMT, in which N-doped CNTs are grown on the Co particles that catalyze their formation through thermal decomposition of acetonitrile. This process constructs multidimensional MPZ-CC@CNT on the basis of the 2D nanoridge and decorated it with 0D multiple metallic seeds and 1D grafted CNT, which also changes the electrode color from purple to black (Figure S2d, Supporting Information). As demonstrated in **Figure 2c, d**, the resulting architecture observed by scanning electron microscopy (SEM) features great similarity to mountain ridges in the macroscopic scale. Bending tests show no detachment of the as-grown nanoridges from NF, suggesting strong adhesion and integration between the material

and substrate (Figure S2e, Supporting Information). The ZnCo-HMT is crucial to the construction of such hierarchical architecture as it not only offers ordered groundwork for the growth of CNT during pyrolysis, but also provides homogeneously embedded Co nanoparticles that catalyze the CNT growth on both sides of these nanoridges. The CNT content in the obtained MPZ-CC@CNT is optimized by manipulating the acetonitrile dosages. It is observed that the CNT content rises with increasing amount of acetonitrile and 3 mL acetonitrile is found to be the optimal dosage to provide ideal CNT nanoridge (Figures S7 and S8, Supporting Information).

The XRD pattern of the MPZ-CC@CNT suggests the disappearance of ZnCo-HMT phase and a new reflection peak at 26° attributed to the (002) facet of highly graphitized CNT (Figure S9a, Supporting Information). The powder sample is also scraped off from the substrate to confirm their XRD pattern. The results show three peaks located at 44°, 51°, and 75° (Figure S9b, Supporting Information), corresponding to (111), (200), and (220) crystal planes of cubic metallic Co, confirming the formation of Co in the final

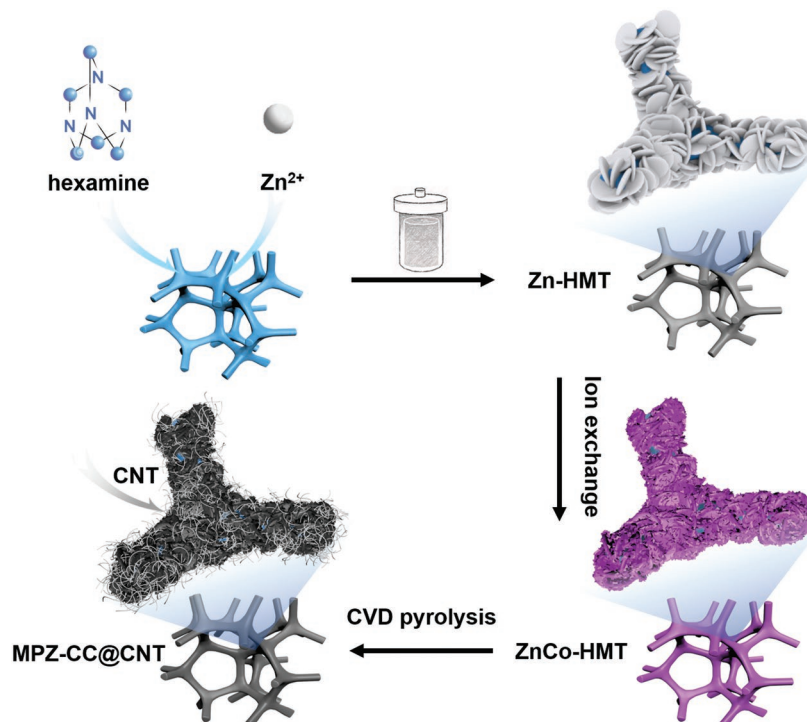


Figure 1. Schematic of the preparation process for MPZ-CC@CNT.

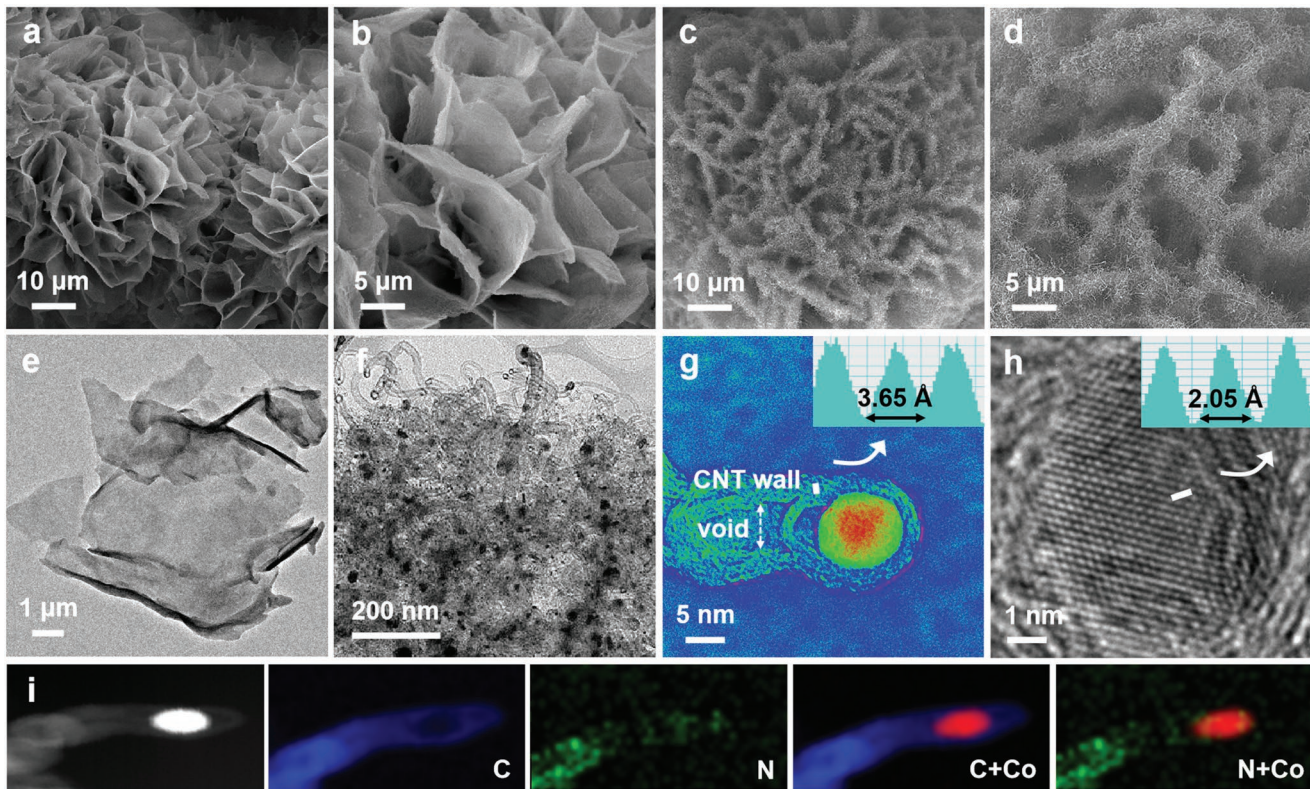


Figure 2. SEM images of the a,b) ZnCo-HMT and c,d) MPZ-CC@CNT. TEM image of e) ZnCo-HMT and f) MPZ-CC@CNT. HRTEM images of the g) CNT and h) Co nanoparticles with inset showing corresponding line profiles along the marked line in g) and h). i) STEM and EELS elemental mapping of MPZ-CC@CNT.

hybrids. A great number of CNTs with length up to several hundreds of nanometers are observed by SEM to be tightly grafted on both sides of nanoridge, generating elongate and vertically hybrid arrays as shown in Figure 2d. Transmission electron microscopy (TEM) image in Figure 2f affirms the presence of the Co nanoparticles with average diameter of ≈ 11 nm (Figure S10, Supporting Information) underneath the CNTs. While high-resolution TEM (HRTEM) image reveals the CNT to have multiwall features and outer diameters ranging from 10 to 20 nm (Figure 2g). The interlayer spacing of the graphitic walls is around 0.365 nm (white lines in Figure 2g), which is attributed to the (002) lattice plane of CNT. As for the lattice fringes in Figure 2h, they reveal the characteristic lattice spacing of 0.205 nm corresponding to Co (111) plane, which is also in accord with the XRD analysis (Figure S9, Supporting Information). The formation of CNT on Co nanoparticles follows the typical vapor liquid-solid growth mode.^[35] The diffusion of carbon atoms start around the Co nanoparticles embedded in nanoridges at high temperature, and then the supersaturation of the dissolved carbon atoms induces the formation of CNTs.^[36] The CNTs growth results in rich amount of pores on nanoridges as shown in Figure S11 in the Supporting Information, which is further corroborated by the HRTEM image of the acid-leached MPZ-CC@CNT (Figure S12, Supporting Information). In contrast, ZnCo-HMT without acetonitrile injection at 950 °C yields Co nanoparticles embedded in carbon nanoridges (denoted as CC) with nonporous structure (Figure S13, Supporting Information).

N_2 adsorption-desorption isotherms and pore size distribution confirm the hierarchical porosity of MPZ-CC@CNT (Figure 3a). In comparison, the isotherms of CC show a barely distinguishable hysteresis loop due to its nonporous structure. The Brunauer–Emmett–Teller (BET) surface area of MPZ-CC@CNT is measured to be $62.0\text{ m}^2\text{ g}^{-1}$ which is much higher than those of CC ($23.3\text{ m}^2\text{ g}^{-1}$), pure CNT ($11.3\text{ m}^2\text{ g}^{-1}$), and pure NF ($1.2\text{ m}^2\text{ g}^{-1}$), verifying the promoting effects of the in situ hybridization of CNT and Co embedded nanoridge in such hierarchical porosity. Specifically, the micropores in the carbon nanoridge are generated by evaporation of Zn nanoparticles, while the mesopores are formed around Co nanoparticles that catalyze the carbon graphitization and CNT growth.^[18,19,37] These micropores and mesopores in MPZ-CC@CNT are expected to elongate oxygen molecules trapping periods and enhance its interactions with catalytically active sites.^[38] Benefiting from the open and ordered nanoridge arrays and skeleton of NF, the macropores enable ample gas–solid–liquid triphasic interfaces and bidirectional gas channels for oxygen evolution and consumption. For comparison, a densely packed architecture with “prohibited zones” (denoted as PZ-CC@CNT) derived from conventional nanopolyhedral ZnCo-bimetal organic framework grown on NF is prepared (ZnCo-MOF), which exhibits much weaker adsorption behavior (Figure 3a, and Figure S14, Supporting Information).

Scanning TEM and electron energy loss spectroscopy mappings (STEM-EELS) of the CNT show uniform distribution of N along the tube, indicative of the simultaneous decoration of

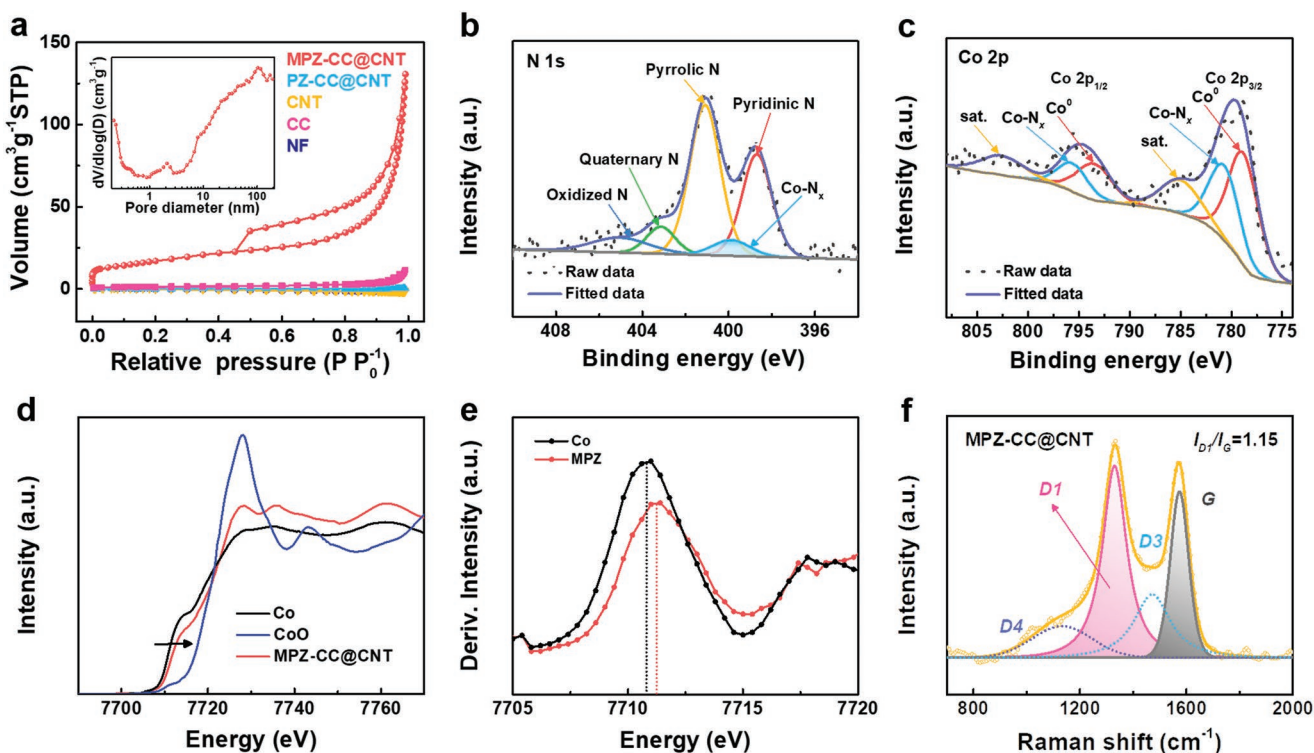


Figure 3. a) N_2 adsorption–desorption isotherm and pore size distribution, the experimental and fitted high-resolution XPS spectra of b) N 1s, c) Co 2p for MPZ-CC@CNT. d) XANES, and e) the first derivative of XANES at Co K-edge. f) Raman spectra for MPZ-CC@CNT.

N on the CNT as discussed above (Figure 2i). This decoration is further confirmed by XPS, wherein the N concentration of MPZ-CC@CNT is measured to be 9.37% (Figure S15 and Table S1, Supporting Information). The high level of N dopants in MPZ-CC@CNT likely originates from the gas source or the N in the HMT ligands ($N/C = 66.7\%$). STEM-EELS (Figure 2i) of the Co nanoparticles reveal the high likelihood of Co atoms in the CNT being adjacent to N atoms, suggesting possible chemical bonding of Co-N_x in the carbon lattices. The Co-N_x configuration in MPZ-CC@CNT is verified by high-resolution N 1s XPS spectrum that shows a minor peak at 399.8 eV representing the N interaction with Co (Figure 3b). The Co 2p spectrum demonstrates the presence of both zero-valence state and ionic state Co species, which are derived from metallic Co and Co-N_x coordination, respectively (Figure 3c). The Co electronic state is further studied by the Co K-edge X-ray absorption near-edge structure (XANES) spectra. As shown in Figure 3d, the Co K-edge absorption edge position of MPZ-CC@CNT appears between those of pure Co and CoO, indicating a Co valence between Co⁰ and Co²⁺.^[39] Additionally, the first derivative XANES spectra in Figure 3e shows the Co white line peak of MPZ-CC@CNT exhibits a small shift to the higher energy compared to that of pure Co, likely due to the strong coupling between Co and CNT through the Co-N_x coordination.^[40]

Such chemical bonding configuration of Co-N_x can create additional defects in the carbon lattices, which is identified by the Raman spectra. As shown in Figure 3f and Figure S16 in the Supporting Information, the Raman spectra are deconvoluted to four bands for in-depth investigation. These four bands include the D1 band with A_{1g} symmetry vibration mode

corresponding to the disorder and imperfect crystallite grains of graphite, the D3 band assigned to sp^3 amorphous carbon, the D4 band representing polyene-like or defective structures, and the G band associated with defect free sp^2 carbon networks with E_{2g} symmetry vibration mode.^[41] The higher I_{D1}/I_G ratio of MPZ-CC@CNT indicates its more defective surface with respect to pure CNT (1.15 versus 0.72). While the different I_{D4}/I_G ratio of MPZ-CC@CNT (0.20) and CNT (0.10) indicates the presence of additional polyene-like defects in MPZ-CC@CNT. Altogether, incorporation of Co into the carbon frameworks and enrichment of defects generated by N-doping and Co-N_x are anticipated to synergistically boost the catalytic performance of MPZ-CC@CNT.^[42] Specifically, these components reduce electron density of neighboring C atoms, which promotes the capturing of oxygen involved reactants and assures fast electrocatalytic oxygen redox kinetics for ORR and OER.^[12,43]

2.2. Electrochemical Evaluation

Inspired by the unique structure and surface chemistry, the obtained self-supported MPZ-CC@CNT is directly applied as the bifunctional electrode for ORR and OER. Commercial state-of-the-art 20 wt. % Pt/C and 20 wt. % Ir/C catalysts are also dip-coated onto NF (denoted as Pt/C and Ir/C, respectively) with the same loading (1 mg cm^{-2}) as MPZ-CC@CNT and served as ORR and OER benchmarks, respectively. To highlight the structural superiority of MPZ-CC@CNT, three other electrodes are also fabricated for comparison: 1) CC (Figure S13, Supporting

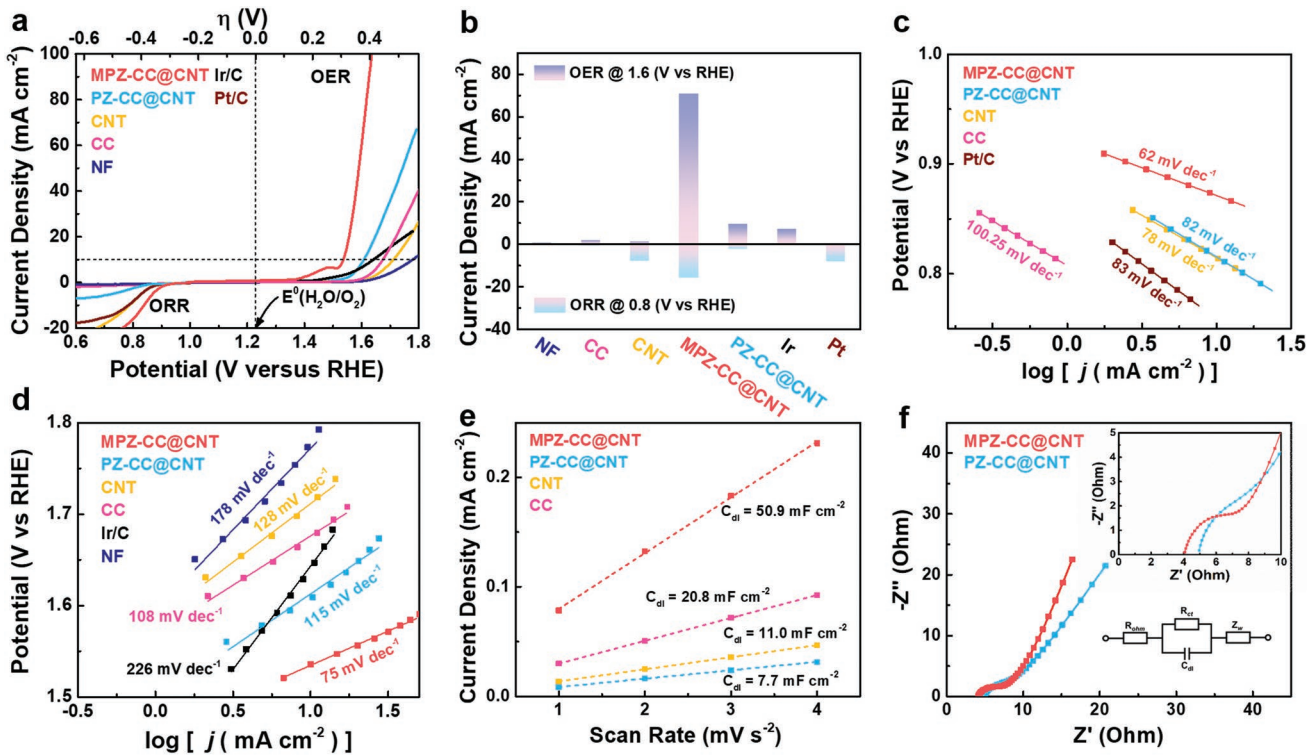


Figure 4. a) ORR and OER polarization curves and b) specific current density. c) ORR and d) OER Tafel plots of different air electrodes in 0.1 M KOH. e) Plots of current densities (taken at 1.05 V) as a function of scan rates. f) The EIS analysis of electrolyte-infiltrated MPZ-CC@CNT and PZ-CC@CNT. R_{ohm} : ohmic resistances, R_{ct} : charge-transfer resistance, C_{dl} : interfacial capacitance, and Z''_w : Warburg diffusion impedance.

Information), 2) PZ-CC@CNT (Figure S14, Supporting Information), and 3) CNT (Figure S17, Supporting Information). Steady-state linear sweep voltammetry (LSV) within 0.1 M KOH electrolyte is adopted to verify their electrocatalytic performance.

The steady-state iR-compensated polarization curves of all tested electrodes are shown in **Figure 4a**. The bare NF shows very poor ORR activity with negligible cathodic current density (black line in Figure 4a). In comparison, MPZ-CC@CNT manifests substantial improvement in ORR activity, showing a more positive onset potential ($E_{\text{onset}} = 0.95$ V versus reversible hydrogen electrode (RHE), measured at -0.1 mA cm^{-2} and higher current density at 0.8 V, Table S2, Supporting Information). As for the OER performance, the overpotential for water electrolyzes at a current density of 10.0 mA cm^{-2} ($\eta_{j=10}$) is a metric to assess OER activity. The OER catalytic activity for MPZ-CC@CNT is also higher than the reference samples, requiring the lowest $\eta_{j=10}$ of 300 mV. Moreover, both the oxygen reduction and evolution currents of as-designed MPZ-CC@CNT are 10–50-folds higher than all the electrodes studied (Figure 4b), indicative of fast electrochemical oxygen redox reaction kinetics. This is further supported by the calculated Tafel slopes in Figure 4c, d, where MPZ-CC@CNT exhibits the smallest values for both ORR (62 mV dec^{-1}) and OER (75 mV dec^{-1}). The results reveal that the open and ordered architecture of MPZ-CC@CNT leads to superior ORR and OER kinetics on the electrolyte-catalyst surface, which is attributed to the accelerated bidirectional transportation of the reactants, i.e., flash reactants shuttling. The significance of the open and order structure is further confirmed by the LSVs measurement

of increased overpotential and decreased current density for the PZ-CC@CNT electrode with densely packed structure.

Further electrochemical analyses are performed to verify the benefits of MPZ-CC@CNT in terms of ample catalyst/electrolyte interface for catalytic sites and fast reactants shuttling. The electrochemical double-layer capacitance (C_{dl}) and the electrochemical active surface area (ECSA) are calculated by measuring the cyclic voltammetry (CV) curves in a non-Faradic potential range (Figure S18, Supporting Information).^[44,45] As shown in Figure 4e, in comparison to CC (20.8 mF cm^{-2}), CNT (11.0 mF cm^{-2}), and PZ-CC@CNT (7.7 mF cm^{-2}), the expanded C_{dl} of MPZ-CC@CNT (50.9 mF cm^{-2}) indicates its higher ECSA, implying that the reactive sites of MPZ-CC@CNT are much more accessible compared to PZ-CC@CNT. This is further supported by electrochemical impedance spectroscopy (EIS) measured in 0.1 M KOH (Figure 4f). From the Nyquist plots, both samples demonstrate a semicircle in the high-medium-frequency region and an inclined line at low frequency. Importantly, the MPZ-CC@CNT has a smaller x -intercept, which indicates lower internal and electrode/electrolyte surface resistance.^[12,15,46] Meanwhile, the steeper slope in low-frequency range implies faster mass diffusion within the optimized electrode/electrolyte interface due to the open and ordered structure.^[47,48] These results mutually confirm that the catalytic active sites had more access to the triphasic interface and smooth reactants pathways for evolution and consumption benefiting from reduced “prohibited zones” offered by MPZ-CC@CNT, which enables fast oxygen electrochemistry (Figure S19, Supporting Information).

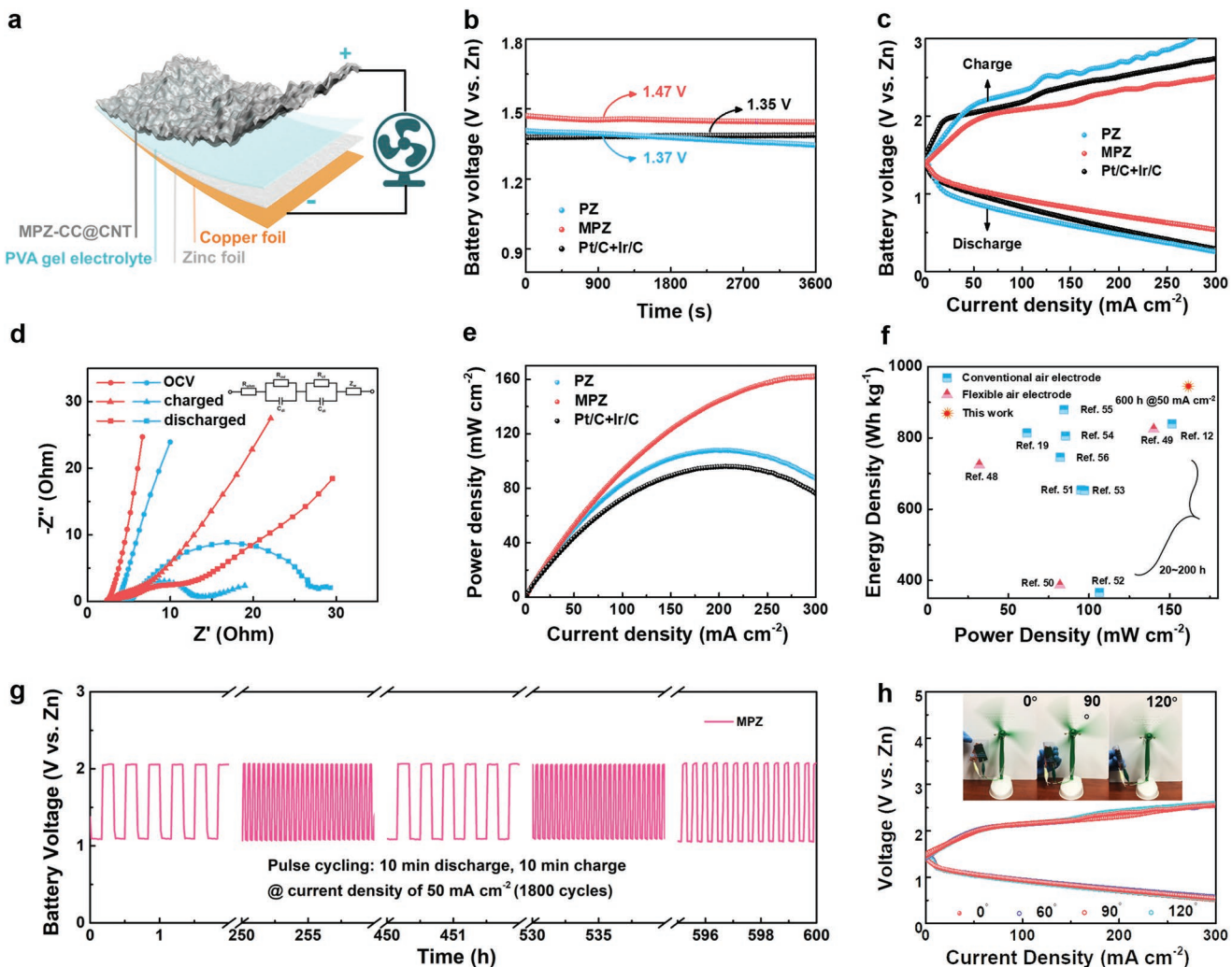


Figure 5. a) Schematic illustration and demonstration of the quasi-solid-state, flexible, and rechargeable ZAB. b) Average OCV, c) charge and discharge polarization curves, d) Nyquist plots (blue: PZ and red: MPZ) measured at different states, within the frequency range from 0.05 Hz to 100 kHz, e) power density plots for ZAB with various air cathodes. f) Comparison of the energy density and power density. g) Galvanostatic cycling stability of ZAB with MPZ-CC@CNT. h) Polarization curves of the battery using the MPZ-CC@CNT air electrode under various bending conditions.

The practical application of rechargeable FZABs requires excellent electrochemical stability, which is examined by chronoaamperometric (CA) measurements. At a constant voltage of 0.75 V, the MPZ-CC@CNT retains 93.2% of its ORR current density after 48 h of continuous operation, whereas the commercial Pt/C catalysts only maintain 75.6% of its original value (Figure S20a, Supporting Information). Similarly, robust OER stability is also demonstrated by MPZ-CC@CNT whose current density reduces by only 4.9% after 48 h at 1.55 V, whereas the Ir/C electrode suffers a sharp decay of 24.7% in current density (Figure S20b, Supporting Information). After the CA test, the MPZ-CC@CNT shows negligible losses in activity in comparison to the noble-metal benchmarks (Figure S20c, Supporting Information). The electrocatalytic stability at a higher current density (100 mA cm^{-2}) of MPZ-CC@CNT is also evaluated, which does not show obvious overpotential shift after 75 000 s of continuous operation (Figure S21, Supporting Information).

Building on the promising bifunctional electrocatalytic activity and stability presented above, we further examine the feasibility of the self-supported MPZ-CC@CNT in FZABs (denoted as MPZ battery) with gel alkaline poly(vinyl-alcohol) (PVA) membrane as the electrolyte (Figure 5a and Figure S22, Supporting Information). For comparison, FZABs using PZ-CC@CNT electrode (PZ battery) and commercial Pt/C+Ir/C catalyst mixture as air electrode (PI battery) are also fabricated following the same procedure. The MPZ battery provides an open circuit voltage (OCV) of 1.47 V that is higher than PI battery (1.35 V) and PZ battery (1.37 V, Figure 5b), indicating lower catalytic activation loss. Figure 5c displays the charge and discharge polarization curves of the three rechargeable batteries. Some turbulences are observed in the polarization curve during charging due to vigorous oxygen bubble coalescence at high current densities. It clearly reveals that both curves of the MPZ battery exhibit lower overpotential than those of PI and PZ battery especially at high current densities,

evidencing the fast kinetics of oxygen reactions. This is also supported by ex situ EIS analysis of the MPZ and PZ batteries under OCV, discharged and charged states. The battery impedances are composed of three components in the EIS spectra: 1) a high frequency incomplete mainly corresponding to OH⁻ transport behavior (R_{int}) at the electrodes/electrolyte interface; 2) a medium-frequency semicircle representing the charge-transfer resistance (R_{ct}) in parallel to the electrode double layer capacitance; and 3) a low-frequency tail attributed to the mass transport limitations (Z_w) of reactants (i.e., oxygen, water, and zinc species). As shown in Figure 5d, R_{ct} of both electrodes experience growth after discharge and then charge, and the slopes of the tails at the low frequency are less steep compared with that measured at OCV state, which is likely caused by the deposition of ZnO on the air electrode during the cycling process.^[49] Moreover, it is noteworthy that the impedances (R_{ct} and Z_w) of MPZ-CC@CNT is much lower than those of PZ-CC@CNT electrode, implying the reduced internal resistance and fast oxygen electrochemical redox within MPZ-CC@CNT, which can be attributed to the capability of the open structure in accommodating the deposition of ZnO during the cycling. As a result of the excellent kinetics, MPZ battery is capable of delivering narrow average charge-discharge voltage gap even when the current rate is increased to 80 or 100 mA cm⁻² (Figure S23, Supporting Information). The prominent electrochemical performance of the MPZ-CC@CNT air electrode is further evidenced by its high peak power density, which is substantially enhanced compared to those of PI battery and PZ battery (Figure 5e). Additionally, specific capacity (normalized to the mass of the zinc electrode) of the primary MPZ battery is about 860 mA h g⁻¹ when discharged at a current density of 25 mA cm⁻². The corresponding gravimetric energy density of MPZ battery is about 946 Wh kg⁻¹, which is much higher than that of PI battery (722 Wh kg⁻¹; Figure S24, Supporting Information) and even exceeds those of most recent results on bifunctional electrocatalysts (Figure 5f).^[12,19,50–58]

Stability of the MPZ and PI batteries are also examined at a high current density of 50 mA cm⁻² with cycle period of 20 min. The PI battery experiences conspicuous voltage gap increases, growing from 1.08 to 1.86 V after 33 h (Figure S25, Supporting Information). In comparison, the voltage gap of the battery using MPZ-CC@CNT electrode increases only by 10 mV (from 0.97 to 0.98 V) after 600 h, representing excellent cycling stability with an extremely low voltage fading rate of 0.006 mV per cycle (Figure 5g and Figure S26, Supporting Information), which is highly competitive among cobalt-based air electrodes in recent literatures (Table S3, Supporting Information). Post-cycling SEM and TEM images of the cycled MPZ-CC@CNT electrode confirm that the open and unstacked structure remained intact. The original size and morphology of the Co nanoparticles are also observed to be well maintained inside the graphitized carbon shell without obvious agglomeration or detachment (Figure S27, Supporting Information).

In addition to the outstanding cycle stability, the MPZ battery shows great potentials for flexible and wearable electronic applications. The charge and discharge profiles of the MPZ battery under various bending conditions and current densities are shown in Figure 5h. The voltage gaps of the battery remain virtually unchanged at any given bending angles, which again

reveals that MPZ-CC@CNT electrode possess high flexibility to efficiently deliver reactants from/to the gas-liquid-solid interface for enhanced catalytic reaction within its ordered architecture. The prospective bendable application of this device is further demonstrated in Figure 5h, with the MPZ battery powering an electric fan under various bending conditions.

3. Conclusion

In this work, a novel air electrode MPZ-CC@CNT with open and ordered array assembled by 1D CNT and 2D carbon nanoridges decorated with 0D cobalt nanoparticles is designed for high-energy density FZABs. The unique MPZ-CC@CNT electrode possesses open and unpacked nano-architecture and achieves intimate covalently coupling between the multidimensional components, leading to both optimal active site utilization and robust stability, thus flash electrocatalytic kinetic and long-term stability are realized in quasi-solid-state FZABs. The outstanding FZAB performance on MPZ-CC@CNT electrode is ascribed to its three major advantages: the order-arrayed architecture allowing the formation of desirable triphasic interfaces for oxygen electrocatalysis with minimized “prohibited zones”, providing sufficient electrocatalytic sites and flash diffusion shuttling for the reactants and intermediates; the Co-N_x sites favoring the capture of oxygen species and thus accelerating the kinetics of ORR and OER; and the space-confined CNT helping to alleviate the Co nanoparticles agglomeration and thus resulting in salient stability.

4. Experimental Section

Chemicals: Hexamine (99%, Analytical grade), zinc nitrite hexahydrate (99%, Analytical grade), zinc acetate tetrahydrate (99%, Analytical grade), cobalt nitrite hexahydrate (99%, Analytical grade), potassium hydroxide (85%, Analytical grade), methanol (99.9%, anhydrous), and ethanol (99.9%, anhydrous) were purchased from Sigma-Aldrich. Nafion dispersion (5 wt. % in ethanol) was bought from Ion Power Inc. All chemicals were used without further purification. The deionized water (18 MΩ) was obtained from a Millipore System.

Synthesis of Zn-HMT and ZnCo-HMT: 0.65 g Zn(NO₃)₂·6H₂O was first dissolved in 15 mL methanol solution; the solution was then added to another 10 mL methanol containing 1.35 g hexamine under vigorous stirring. The mixture was then transferred into an autoclave reactor and heated for 24 h at 60 °C with cleaned NF (2 × 5 cm) placed within the solution as substrates for the product. After that, the white product, labeled as Zn-HMT, was washed by deionized water and dried in ambient air. The as-prepared Zn-HMT was then immersed into a beaker containing 1.30 g cobalt nitrate and 25.0 mL ethanol for 12 h at room temperature to obtain ZnCo-HMT.

Synthesis of CC, CNT, PZ-CC@CNT, and MPZ-CC@CNT: The MPZ-CC@CNT was obtained by applying a CVD process following the thermostatic carbonization process of ZnCo-HMT at 950 °C in Ar for 2 h with a ramping rate of 5 °C min⁻¹ by using acetonitrile as the gas precursor without any additional catalyst. As a control experiment, CC was also fabricated under similar conditions in the absence of acetonitrile. The CNT was obtained by applying a CVD process using acetonitrile as the gas precursor with catalyst at 950 °C in Ar for 2 h with a ramping rate of 5 °C min⁻¹. The PZ-CC@CNT was obtained by applying a similar CVD process following the thermostatic carbonization process of nanopolyhedral ZnCo-MOF. The ZnCo-MOF are prepared according to the previously reported procedures.^[1] In a typical synthesis procedure,

1 mmol Zn(NO₃)₂·6H₂O and 3 mmol of 2-methylimidazole were added into 15 and 10 mL of methanol, respectively. After they were totally dissolved, the latter solution was added into the former under magnetic agitation for 1 min and then transferred into an autoclave reactor and heated for 24 h at 60 °C with cleaned NF (2 × 5 cm) placed within the solution as substrates for the product. After that, the purple product, labeled as ZnCo-MOF, was washed by deionized water and dried in ambient air.

Fabrication of Flexible Zn-Air Battery: The as-prepared electrodes were directly used as the air cathodes and zinc foils were polished to be used as the anodes. Commercial state-of-art 20 wt.% Pt/C and Ir/C nanocomposites were used as the bifunctional electroactive material to fabricate the reference air cathode. Homogeneous catalyst ink consisting of the nanocomposites, ionomer (Nafion solution, 5 wt. %) and ethanol was sprayed onto a nickel powder-based gas diffusion layer (GDL) with a catalyst loading of 1 mg cm⁻². The nickel powder-based GDL was prepared by a single-layering method, where all components were mixed and compressed together onto NF. The components including nickel powder and poly(tetrafluoroethylene) were put into a mixture of distilled water and 2-propanol, and then ultrasonicated for 2 h so as to achieve uniformly dispersed solution. With being dried by nitrogen gas stream at ambient temperature, the prepared slurry was obtained and put onto the NF covering a side. After the process, the coated-NF was compressed by rolling press. The interparticle voids that formed between the nickel particle acted as the GDL. This type of nickel powder based GDL has been proven to be effective in previously reported articles, particularly for rechargeable metal-air battery applications, where conventional carbon-based GDLs tend to undergo carbon corrosion due to high potentials incurred during battery charging.^[2,3] The alkaline gel electrolyte was prepared by dissolving KOH, Zn(CH₃COO)₂ and PVA in deionized water at 90 °C under vigorous stirring until the solution became clear. The in-house battery prototype was fabricated through a layer-by-layer method by which the electrodes were placed face-to-face with the alkaline gel polymer.

Materials Characterization: The morphology and structure were imaged by TEM (JEOL, JEM-2010, 200 kV). XRD patterns were obtained by a Bruker AXS D8 APZance powder X-ray diffractometer equipped with a Cu K α radiation source ($\lambda = 1.5406\text{\AA}$) and a graphite monochromator. XPS measurements were carried out by a Thermal Scientific K-Alpha XPS spectrometer. A Gaussian–Lorentzian mix is used while analyzing XPS peaks. The background used was the “Shirley” background. The binding energy scale was calibrated to fix the carbon sp³ peak at 284.8 eV.^[4,5] Co K-edge XANES measurements were performed at Canadian Light Source Inc, Canada, using the SXRMB beamline. Reference compounds, such as metal foils and oxides were measured in total electron and transmission modes for comparison and energy calibration. All XANES data were processed using Athena program. The pore structure was investigated by N₂ adsorption–desorption measurements on a BET surface area analyzer (Quantachrome Instruments QuadraSorb SI4) and a Barrett–Joyner–Halenda model was used to obtain pore size distribution. Raman spectroscopy was conducted on Renishaw inVia plus (Renishaw, UK) using laser excitation at 532 nm.

Electrochemical Measurement: The electrochemical measurements were performed in a three-electrode system with an electrochemical workstation (Biologic VMP-3). The electrocatalytic performances for ORR and OER reactions were measured in a three-electrode cell at standard temperature and pressure conditions. The CC, CNT, PZ-CC@CNT, and MPZ-CC@CNT were directly used as the working electrodes. A graphite rod and an RHE are selected to be the counter and reference electrodes, respectively. Commercial Pt/C (20 wt.% Pt) and Ir/C (20 wt.% Ir) catalysts were used as the reference materials and prepared by mixing 4 mg of the catalyst in 1000 μL of ethanol containing 0.15 wt.% Nafion dispersion, followed by ultrasonication for 1 h to obtain a homogeneous ink. Then as-prepared ink was dropped onto the NF surface with same catalyst loading of 1 mg cm⁻² for Pt/C and Ir/C catalysts. All the measurements were carried out in 0.1 M KOH solution, where O₂ or N₂ gas was purged for 30 min before ORR or OER measurements, respectively. The LSV measurements were performed from 1.0 to 0.1 V (versus RHE) for ORR

and from 1.0 to 1.8 V (versus RHE) for OER with scan rate of 10 mV s⁻¹. ORR and OER polarization curves were corrected by IR-compensation in 0.1 M KOH solution, where the resistance is determined by the high-frequency intercept from the Nyquist plot acquired from EIS. EIS was recorded by Gamry 5000E work station in the frequency range of 0.1 Hz–100 kHz. The C_{dl} was calculated from double-layer charging curves in a non-faradic potential range of 1.1–1.3 V (versus RHE) and using the following equation in which i_c and v are charging current (mA cm⁻²) and scan rate (mV s⁻¹), respectively^[6–10]:

$$i_c = v C_{dl}$$

The stability test was carried out using CV between 0.7 and 1.7 V (versus RHE) in O₂-saturated 0.1 M KOH solution at 50 mV s⁻¹. The stability studies on the half-cell reactions (ORR and OER separately) was primarily assessed by CA measurements at a given constant potential for 48 h. Galvanostatic discharge and charge cycling of the ZABs was performed through a recurrent galvanostatic pulse method at a current density of 50 mA cm⁻² with 20 min per cycle. Rate capabilities were investigated by galvanostatic charge-discharge measurements at various current densities from 10 to 100 mA cm⁻². These galvanostatic charge/discharge curves were recorded using a LAND battery testing station (CT2001A) at room temperature. Polarization data were collected using the galvanodynamic method at a scan rate of 1.0 mA s⁻¹.

Supporting Information

Supporting Information is available from the Wiley Online Library or from the author.

Acknowledgements

This work was financially supported by the Natural Sciences and Engineering Research Council of Canada (NSERC), the University of Waterloo, and the Waterloo Institute for Nanotechnology. The authors also thank the Dr. Qunfeng Xiao from Canadian Light Source (CLS) for XANES measurement. The CLS is supported by the NSERC, the National Research Council Canada, the Canadian Institutes of Health Research, the Province of Saskatchewan, Western Economic Diversification Canada, and the University of Saskatchewan.

Conflict of Interest

The authors declare no conflict of interest.

Keywords

flash reactants shuttling, multidimensional ordered architecture, self-supported electrodes, Zn-air batteries

Received: March 19, 2019

Revised: April 12, 2019

Published online:

- [1] J. Fu, F. M. Hassan, C. Zhong, J. Lu, H. Liu, A. Yu, Z. Chen, *Adv. Mater.* **2017**, *29*, 1702526.
- [2] J. Fu, R. Liang, G. Liu, A. Yu, Z. Bai, L. Yang, Z. Chen, *Adv. Mater.* **2018**, *1805230*.
- [3] J. Fu, Z. P. Cano, M. G. Park, A. Yu, M. Fowler, Z. Chen, *Adv. Mater.* **2017**, *29*, 1604685.

- [4] D. U. Lee, J.-Y. Choi, K. Feng, H. W. Park, Z. Chen, *Adv. Energy Mater.* **2014**, *4*, 1301389.
- [5] Y. Li, J. Fu, C. Zhong, T. Wu, Z. Chen, W. Hu, K. Armine, J. Lu, *Adv. Energy Mater.* **2019**, *9*, 1802605.
- [6] J. Zhou, X. Li, C. Yang, Y. Li, K. Guo, J. Cheng, D. Yuan, C. Song, J. Lu, B. Wang, *Adv. Mater.* **2019**, *31*, 1804439.
- [7] Y. Liu, G. Li, J. Fu, Z. Chen, X. Peng, *Angew. Chem., Int. Ed.* **2017**, *56*, 6176.
- [8] Y. Li, J. Lu, *ACS Energy Lett.* **2017**, *2*, 1370.
- [9] G. Liu, J. Li, J. Fu, G. Jiang, G. Lui, D. Luo, Y. P. Deng, J. Zhang, Z. P. Cano, A. Yu, D. Su, Z. Bai, L. Yang, Z. Chen, *Adv. Mater.* **2019**, *31*, 1806761.
- [10] H.-F. Wang, C. Tang, Q. Zhang, *Adv. Funct. Mater.* **2018**, *28*, 1803329.
- [11] H. Yang, B. Wang, H. Li, B. Ni, K. Wang, Q. Zhang, X. Wang, *Adv. Energy Mater.* **2018**, *8*, 1801839.
- [12] C. Tang, B. Wang, H. F. Wang, Q. Zhang, *Adv. Mater.* **2017**, *29*, 1703185.
- [13] Q. Liu, Z. Chang, Z. Li, X. Zhang, *Small Methods* **2018**, *2*, 1700231.
- [14] P. Li, H. Jang, J. Zhang, M. Tian, S. Chen, B. Yuan, Z. Wu, X. Liu, J. Cho, *ChemElectroChem* **2019**, *6*, 393.
- [15] H.-F. Wang, C. Tang, B. Wang, B.-Q. Li, X. Cui, Q. Zhang, *Energy Storage Mater.* **2018**, *15*, 124.
- [16] H. J. Peng, J. Q. Huang, Q. Zhang, *Chem. Soc. Rev.* **2017**, *46*, 5237.
- [17] W. Liu, J. Zhang, Z. Bai, G. Jiang, M. Li, K. Feng, L. Yang, Y. Ding, T. Yu, Z. Chen, A. Yu, *Adv. Funct. Mater.* **2018**, *28*, 1706675.
- [18] Y. Jiang, Y.-P. Deng, J. Fu, D. U. Lee, R. Liang, Z. P. Cano, Y. Liu, Z. Bai, S. Hwang, L. Yang, D. Su, W. Chu, Z. Chen, *Adv. Energy Mater.* **2018**, *8*, 1702900.
- [19] Y. Wang, L. Tao, Z. Xiao, R. Chen, Z. Jiang, S. Wang, *Adv. Funct. Mater.* **2018**, *28*, 1705356.
- [20] T. Wang, G. Nam, Y. Jin, X. Wang, P. Ren, M. G. Kim, J. Liang, X. Wen, H. Jang, J. Han, Y. Huang, Q. Li, J. Cho, *Adv. Mater.* **2018**, *30*, 1800757.
- [21] Q. Qin, H. Jang, P. Li, B. Yuan, X. Liu, J. Cho, *Adv. Energy Mater.* **2019**, *9*, 1803312.
- [22] Y.-P. Deng, Y. Jiang, D. Luo, J. Fu, R. Liang, S. Cheng, Z. Bai, Y. Liu, W. Lei, L. Yang, J. Zhu, Z. Chen, *ACS Energy Lett.* **2017**, *2*, 2706.
- [23] K. Huang, Z. Dong, Q. Li, W. Jin, *Chem. Commun.* **2013**, *49*, 10326.
- [24] Y. Hu, J. Wei, Y. Liang, H. Zhang, X. Zhang, W. Shen, H. Wang, *Angew. Chem., Int. Ed.* **2016**, *55*, 2048.
- [25] X. Cao, B. Zheng, X. Rui, W. Shi, Q. Yan, H. Zhang, *Angew. Chem., Int. Ed.* **2014**, *53*, 1404.
- [26] Y. L. Ding, P. Kopold, K. Hahn, P. A. van Aken, J. Maier, Y. Yu, *Adv. Mater.* **2016**, *28*, 7774.
- [27] J.-S. Lee, S. Tai Kim, R. Cao, N.-S. Choi, M. Liu, K. T. Lee, J. Cho, *Adv. Energy Mater.* **2011**, *1*, 34.
- [28] W. Ahn, M. G. Park, D. U. Lee, M. H. Seo, G. Jiang, Z. P. Cano, F. M. Hassan, Z. Chen, *Adv. Funct. Mater.* **2018**, *28*, 1802129.
- [29] B. Y. Guan, L. Yu, X. W. Lou, *Energy Environ. Sci.* **2016**, *9*, 3092.
- [30] H. Hu, L. Han, M. Yu, Z. Wang, X. W. D. Lou, *Energy Environ. Sci.* **2016**, *9*, 107.
- [31] D. U. Lee, P. Xu, Z. P. Cano, A. G. Kashkooli, M. G. Park, Z. Chen, *J. Mater. Chem. A* **2016**, *4*, 7107.
- [32] Z.-L. Wang, D. Xu, J.-J. Xu, X.-B. Zhang, *Chem. Soc. Rev.* **2014**, *43*, 7746.
- [33] J.-I. Jung, M. Risch, S. Park, M. G. Kim, G. Nam, H.-Y. Jeong, Y. Shao-Horn, J. Cho, *Energy Environ. Sci.* **2016**, *9*, 176.
- [34] S. Liu, D. Li, G. Zhang, D. Sun, J. Zhou, H. Song, *ACS Appl. Mater. Interfaces* **2018**, *10*, 34193.
- [35] Y. L. Ding, P. Kopold, K. Hahn, P. A. van Aken, J. Maier, Y. Yu, *Adv. Funct. Mater.* **2016**, *26*, 1112.
- [36] A. Rinaldi, J. P. Tessonnier, M. E. Schuster, R. Blume, F. Girgsdies, Q. Zhang, T. Jacob, S. B. Abd Hamid, D. S. Su, R. Schlogl, *Angew. Chem., Int. Ed.* **2011**, *50*, 3313.
- [37] J. Meng, C. Niu, L. Xu, J. Li, X. Liu, X. Wang, Y. Wu, X. Xu, W. Chen, Q. Li, *J. Am. Chem. Soc.* **2017**, *139*, 8212.
- [38] X. Fu, P. Zamani, J. Y. Choi, F. M. Hassan, G. Jiang, D. C. Higgins, Y. Zhang, M. A. Hoque, Z. Chen, *Adv. Mater.* **2017**, *29*, 1604456.
- [39] L. Zhang, J. Fischer, Y. Jia, X. Yan, W. Xu, X. Wang, J. Chen, D. Yang, H. Liu, L. Zhuang, M. Hankel, D. J. Searles, K. Huang, S. Feng, C. L. Brown, X. Yao, *J. Am. Chem. Soc.* **2018**, *140*, 10757.
- [40] B. You, N. Jiang, M. Sheng, S. Gul, J. Yano, Y. Sun, *Chem. Mater.* **2015**, *27*, 7636.
- [41] A. Sadezky, H. Muckenthaler, H. Grothe, R. Niessner, U. Pöschl, *Carbon* **2005**, *43*, 1731.
- [42] Y. Jia, K. Jiang, H. Wang, X. Yao, *Chem* **2019**, *5*, 180.
- [43] Y. Guo, P. Yuan, J. Zhang, Y. Hu, I. S. Amiiyu, X. Wang, J. Zhou, H. Xia, Z. Song, Q. Xu, S. Mu, *ACS Nano* **2018**, *12*, 1894.
- [44] H. Hu, B. Guan, B. Xia, X. W. Lou, J. Am. Chem. Soc. **2015**, *137*, 5590.
- [45] L. Yu, B. Y. Xia, X. Wang, X. W. Lou, *Adv. Mater.* **2016**, *28*, 92.
- [46] C. Tang, L. Zhong, B. Zhang, H. F. Wang, Q. Zhang, *Adv. Mater.* **2018**, *30*, 1705110.
- [47] S. H. Ahn, M. J. Klein, A. Manthiram, *Adv. Energy Mater.* **2017**, *7*, 1601979.
- [48] H. Zou, B. He, P. Kuang, J. Yu, K. Fan, *Adv. Funct. Mater.* **2018**, *28*, 1706917.
- [49] S. Liu, M. Wang, X. Sun, N. Xu, J. Liu, Y. Wang, T. Qian, C. Yan, *Adv. Mater.* **2018**, *30*, 1704898.
- [50] M. Yu, Z. Wang, C. Hou, Z. Wang, C. Liang, C. Zhao, Y. Tong, X. Lu, S. Yang, *Adv. Mater.* **2017**, *29*, 1602868.
- [51] Y. Zhao, Q. Lai, J. Zhu, J. Zhong, Z. Tang, Y. Luo, Y. Liang, *Small* **2018**, *14*, 1704207.
- [52] C. Guan, A. Sumboja, H. Wu, W. Ren, X. Liu, H. Zhang, Z. Liu, C. Cheng, S. J. Pennycook, J. Wang, *Adv. Mater.* **2017**, *29*, 1704117.
- [53] H. Cheng, M.-L. Li, C.-Y. Su, N. Li, Z.-Q. Liu, *Adv. Funct. Mater.* **2017**, *27*, 1701833.
- [54] Z. Song, X. Han, Y. Deng, N. Zhao, W. Hu, C. Zhong, *ACS Appl. Mater. Interfaces* **2017**, *9*, 22694.
- [55] C.-Y. Su, H. Cheng, W. Li, Z.-Q. Liu, N. Li, Z. Hou, F.-Q. Bai, H.-X. Zhang, T.-Y. Ma, *Adv. Energy Mater.* **2017**, *7*, 1602420.
- [56] L. Wei, H. E. Karahan, S. Zhai, H. Liu, X. Chen, Z. Zhou, Y. Lei, Z. Liu, Y. Chen, *Adv. Mater.* **2017**, *29*, 1701410.
- [57] P. Liu, D. Gao, W. Xiao, L. Ma, K. Sun, P. Xi, D. Xue, J. Wang, *Adv. Funct. Mater.* **2018**, *28*, 1706928.
- [58] X. Chen, L. Wei, Y. Wang, S. Zhai, Z. Chen, S. Tan, Z. Zhou, A. K. Ng, X. Liao, Y. Chen, *Energy Storage Mater.* **2018**, *11*, 134.